ROYAL SOCIETY
OF CHEMISTRY

Check for updates

Probing the active sites of a Prussian blue analogue-derived Mn–Co catalyst in the CO hydrogenation to higher alcohols by high-pressure pulse experiments and co-feeding of ethylene

Patrick Diehl,[†] Pascal Telaar,[†‡] Philipp Schwiderowski,[§] Astrid Müller,
Lars Alfes and Martin Muhler [iD] *

The reaction network of higher alcohol synthesis over a pyrolised Prussian blue analogue-based catalyst was investigated by performing transient as well as steady-state kinetic experiments using a Mn-promoted Co catalyst with a molar Mn : Co ratio of 1 : 11 (Mn_1Co_{11}) at 260 °C. While the temperature variation revealed an apparent activation energy of 88 kJ mol^{-1}, the partial pressure variations of CO and H_2 resulted in reaction orders of −0.3 and +0.7 for CO and H_2, respectively. The reaction order for H_2 was similar to the value of +0.8 derived for the previously established 2CoCu catalyst (Co : Cu = 2 : 1) synthesized by co-precipitation, but the activation energy of the Mn_1Co_{11} catalyst was lower by 52 kJ mol^{-1} amounting to only 88 kJ mol^{-1}. While ethylene co-feeding showed that reductive hydroformylation takes place yielding 1-propanol presumably at the Co_2C/Co^0 interface similar to the 2CoCu catalyst, high-pressure pulse experiments using methanol as probe molecule demonstrated the presence of an additional Co-based active site catalyzing the reductive carbonylation of primary alcohols over the Mn_1Co_{11} catalyst. Correspondingly, the presence of Co–N–C sites anchored in the highly nitrogen- and oxygen-functionalized carbon matrix is assumed to result in the intertwined reaction network, comprising the carbide-based mechanism and reductive olefin hydroformylation over Co_2C/Co^0, reductive alcohol carbonylation over the molecular sites and olefin hydration over acidic sites.

Introduction

The heterogeneously catalysed hydrogenation of carbon monoxide to higher alcohols (higher alcohol synthesis, HAS) is a promising key technology to diminish the dependence on fossil fuels, provided that CO and H_2 originate from renewable sources. By synthesising fuel additives without the usage of fossil feedstocks, net CO_2 emissions of this sector can decrease while still guaranteeing to meet the global energy demand.[1,2]

In general, HAS (eqn (1)) can be described by the combination of methanol synthesis (eqn (2)) with Fischer–Tropsch synthesis (FTS, eqn (3) and (4)).[3,4]

Laboratory of Industrial Chemistry, Ruhr University Bochum, Universitätsstraße 150, 44801 Bochum, Germany. E-mail: martin.muhler@ruhr-uni-bochum.de

† These authors contributed equally.

‡ Current affiliation: thyssenkrupp nucera AG & Co. KGaA, Freie-Vogel-Straße 385 a, 44 269 Dortmund, Germany.

§ Current affiliation: Evonik Operations GmbH, Paul-Baumann-Straße 1, 45 764 Marl, Germany.

$$CO + 2n H_2 \rightarrow C_n H_{2n+1}OH + (n-1)\, H_2O \quad (1)$$

$$CO + 2H_2 \rightarrow CH_3OH \quad (2)$$

$$n CO + (2n+1)\, H_2 \rightarrow C_n H_{2n+2} + n H_2O \quad (3)$$

$$n CO + 2n H_2 \rightarrow C_n H_{2n} + n H_2O \quad (4)$$

The combination of these reaction pathways led to a cobalt carbide-based reaction mechanism, which is part of the reaction network we previously proposed for a hydrotalcite-derived Co–Cu-based catalyst (Co : Cu ratio of 2 : 1, 2CoCu).[5,6] Additionally, HAS over catalysts derived from Prussian blue analogue (PBA)-based precursors is influenced by two carbonylation reactions: the carbonylation of methanol (MeOH) to acetic acid (eqn (5)) and the hydroformylation of ethylene to propionaldehyde (eqn (7)). These two reactions were proposed to take place during HAS over PBA-derived catalysts based on the detection of these key intermediates.[7,8]

Both reactions are followed by the fast hydrogenation to the corresponding long-chain alcohol (eqn (6) and (8)).[7]

$$H_3COH + CO \rightarrow H_3CCOOH \tag{5}$$

$$H_3CCOOH \xrightarrow[-H_2O]{+H_2} H_3CCHO \xrightarrow{+H_2} C_2H_5OH \tag{6}$$

$$C_2H_4 \xrightarrow{+CO/H_2} H_5C_2CHO \tag{7}$$

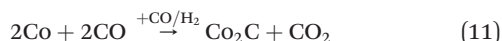$$H_5C_2CHO \xrightarrow{+H_2} C_3H_7OH \tag{8}$$

Beside those reactions, the water-gas shift reaction (WGSR, eqn (9)) as well as the Boudouard equilibrium (eqn (10)) contribute to the discussed HAS reaction network.[3,9,10]

$$CO + H_2O \rightleftharpoons CO_2 + H_2 \tag{9}$$

$$2CO \rightleftharpoons CO_2 + C \tag{10}$$
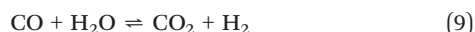
Additionally, recently performed transient kinetic studies on HAS using the 2CoCu catalyst led to the hypothesis that not only the WGSR is leading to the observed formation of CO_2 at HAS conditions, but also an interplay of solid-state reactions involving Co_2C:Co_2C is continuously formed by carbidization releasing CO_2 (eqn (11)) and decomposed by water forming CO_2 and H_2 (eqn (12)) under HAS conditions.[11] Furthermore, carbon formed by the Boudouard equilibrium deposited on the surface can be converted by steam gasification (eqn (13)), which further influences the previously mentioned reactions.[3,9,11,12]

$$2Co + 2CO \xrightarrow{+CO/H_2} Co_2C + CO_2 \tag{11}$$

$$Co_2C + 2H_2O \xrightarrow{+H_2} 2Co + CO_2 + 2H_2 \tag{12}$$

$$C + H_2O \rightarrow CO + H_2 \tag{13}$$

Here, water necessary for the Co_2C decomposition and steam gasification is generated by eqn (1), (3) and (4) describing the formation of higher alcohols (Alc) and hydrocarbons (HC). The solid-state reactions were assumed to be relevant for the PBA-derived catalysts due to the observed structural changes during pyrolysis and under HAS conditions, thereby leading to significant CO_2 formation over these catalysts.[7] In addition, K is known to significantly promote the WGSR over Co_2C,[13] and in our previous study[8] we observed that the removal of K from the PBA-derived catalyst by two different approaches prior to pyrolysis was decreasing but not fully eliminating the formation of CO_2. Therefore, it must be assumed that the solid-state reactions are the main cause for the produced amount of CO_2[8] in addition to unpromoted Co_2C also being active for the WGSR to some extent.[13]

Besides the decreased CO_2 selectivity, both catalysts with lowered K content achieved higher CO conversion, and the catalyst obtained by additional washing also showed a higher total alcohol selectivity of 31%. In contrast, the NH_4-based catalyst strongly resembled FTS catalysts in its catalytic properties, resulting for example in considerable wax formation under reaction conditions. Therefore, the washed catalyst was selected as the so far most promising PBA-based catalyst for HAS.[8]

The proposed intertwined network using PBA-derived Mn–Co-based catalysts originates from the interplay of different active sites, one being the interface between Co_2C and Co^0 sites. As these sites alone would not fully describe the observed product distribution, we proposed the formation of an additional molecular Co-based active site under reaction conditions.[7,8] It has recently been reported that the Co carbonyl hydride complex can be formed at moderate CO partial pressures[14] and it seems reasonable to assume that a similar transformation of Co^0 takes place using PBA-based catalysts. Such a formed complex can be strongly anchored by the highly functionalized carbon matrix, thereby resulting in the formation of Co/N-doped carbon (Co–N–C) sites. Co–N–C[15] and similar sites with different transition metals such as Cu,[16] Fe,[17] or Ni[18] have recently been under investigation to substitute precious metal catalysts in various types of reactions ranging from electrocatalysis[19,20] over photocatalysis[21] to thermocatalytic oxidation,[22] (de-)hydrogenation,[23,24] and carbonylation.[25] In general, this type of catalyst can be obtained by an anaerobic heat treatment of suitable precursors containing carbon, nitrogen, and the desired transition metal.[26–28] The key for this successful transformation is the choice of suitable conditions during the heat treatment, which are reported to be of significant importance for the exact nature of the obtained sites.[29,30] Furthermore, it has been proposed that Co–N–C catalysts can be obtained by pyrolysing a Co-containing PBA as the precursor.[31] Thus, it can be assumed that Co–N–C sites are not only formed using the Mn_1Co_{11} catalyst under HAS conditions, but already during the pyrolysis of the corresponding PBA.

Despite the proposed anchoring of the molecular Co site on the N-functionalized carbon matrix, it is rather likely that a small amount of these molecular Co sites is lost under reaction conditions due to the formation of volatile metal carbonyls.[32–35] For a Cu–Co/ZrO_2 catalyst applied in HAS, it was proposed that the formation of Co_2C might suppress this volatilization.[33] Nonetheless, Co should be detectable in the effluent gas stream if a molecular site is present, which is investigated in this study. Furthermore, Co carbonyl hydride is reported to be strongly acidic,[36] which in turn results in the acidic environment necessary for olefin hydration[37,38] in addition to the influence of the carboxylic acids formed by alcohol carbonylation.

This study further investigates the steady-state kinetics of HAS over the Mn-promoted Co catalyst with a Mn:Co ratio of 1:11 (Mn_1Co_{11}) obtained by the pyrolysis of a washed PBA precursor. To detect the mentioned intermediates during HAS, *in situ* high-pressure diffuse reflectance infrared Fourier transform spectroscopy (DRIFTS) under reaction conditions is a suitable tool with high time-resolution, which is applied during

the heating phase and the induction period of the Mn_1Co_{11} catalyst. Furthermore, co-feeding experiments are performed, and transient kinetics is studied by high-pressure pulse experiments, which have been proven to be a powerful tool to investigate reaction networks in synthesis gas chemistry.[11,39–41] High-pressure pulse experiments have already been established as a surface-sensitive *operando* method for HAS using the 2CoCu catalyst. We were able to show that the 2CoCu catalyst is also an active catalyst for the hydroformylation reaction, provided that a sufficiently high partial pressure of ethylene is applied.[11] Therefore, these pulse experiments were considered suitable to gain insight into the proposed interplay of mechanisms taking place over Mn–Co-based catalysts originating from PBA precursors.

Experimental

Catalyst synthesis and characterization

The applied PBA-based catalyst was synthesised according to the previously applied method,[7] resulting in a PBA precursor with a specific Mn : Co ratio of 1 : 11 after pyrolysis. The microemulsion-assisted co-precipitation was performed at room temperature with an ethanol (EtOH) to H_2O ratio of 1. $Mn(Ac)_2 \cdot 4\ H_2O$ (Aldrich Chemistry, 99%) and $Co(Ac)_2 \cdot 4\ H_2O$ (Sigma-Aldrich, 98%) were dissolved in 150 mL EtOH and 50 mL demineralized water with an excess of 11.12 g polyvinylpyrrolidone (Sigma-Aldrich, PVP-K30). $K_3[Co(CN)_6] \cdot nH_2O$ (Acros Organics, 95%) was dissolved in 100 mL demineralized water and was added dropwise under rigorous stirring. Afterwards, the precipitate was aged for 24 h. The solid PBA precursor was obtained by centrifugation for 10 min at 11 000 rpm. After freeze-drying the precursor for 24 h at −50 °C, the dried precursor was placed on a filter and washed with 3 L distilled water to remove the alkali traces. Then, the washed precursor was freeze-dried again for 48 h at −50 °C. Pyrolysis of the washed and dried precursor was performed for 3 h at 600 °C in a constant flow of N_2 (100 cm^3 min^{-1}) using a heating rate of 2 °C min^{-1}.

X-ray diffraction (XRD) measurements of the spent catalysts were conducted using a Bruker D8 DISCOVER with θ−θ geometry, Cu Kα radiation (λ = 0.15406 nm, 40 kV, 40 mA), and an energy-dispersive LYNXEYE XE-T detector. Angles from 10 to 80° 2θ were measured with a step size of 0.02° and a time per step of 2.0 s. Evaluation of the recorded diffraction patterns was performed using the Diffrac.EVA Software equipped with access to the powder diffraction file 2 (PDF-2) database provided by the International Centre for Diffraction Data (ICDD).

In situ DRIFTS

In situ DRIFTS experiments were performed using a Nicolet NEXUS 670 Fourier transform infrared (FTIR) spectrometer equipped with a PIKE DiffusIR high-temperature heating chamber with integrated sample holder located in a PIKE DiffusIR reflectance accessory which consisted of a fixed mirror system and a height-adjustable monolithic ellipsoidal reflector. A high-pressure module consisting of a ZnSe dome using a Viton O-ring was used to enable operating at pressures in the range of 10^{-6} mbar to 100 bar. The whole setup was purged with pure N_2 at a constant flow rate of 15 L min^{-1} to obtain a constant level of moisture.

All DRIFT spectra were recorded between 800 to 4000 cm^{-1} with a spectral resolution of 4 cm^{-1}, with 256 scans and an aperture setting of 150 using an MCT (mercury cadmium telluride) detector cooled with liquid N_2.

44 mg of the catalyst were placed inside the dome, and pressure was increased with 1 bar min^{-1} to 60 bar using 20 cm^3 min^{-1} He. Afterwards, the sample was heated with 5 °C min^{-1} to 160 °C and slowly with 0.06 °C min^{-1} to 260 °C in He to obtain background spectra.[7,8] After switching to a syngas flow of 20 cm^3 min^{-1} with a H_2 : CO ratio of 1 (H_2 : CO : N_2 = 40 : 40 : 20) at atmospheric pressure and room temperature, the pressure was again increased to 60 bar with a ramp of 1 bar min^{-1} followed by the same heating program.[7,8]

Steady-state kinetics

Steady-state kinetic investigations were conducted in a flow setup equipped with six gas lines.[5] The high-pressure reaction unit of the setup contained a 1/4″ fixed-bed stainless steel reactor equipped with an axial thermocouple in the middle of the catalyst bed. The reactor tube with an inner diameter of 4.5 mm was additionally coated with a thin film of SilcoNert2000®. The reactor was heated by a single-zone furnace. 100 mg of a sieve fraction of 250–355 μm of the pyrolyzed catalyst were filled into the reactor. After the pressure had been increased to 60 bar with 1 bar min^{-1}, the desired flow of 20 cm^3 min^{-1} with the syngas atmosphere of H_2/CO = 1 was established leading to a gas hourly space velocity (GHSV) of 12 000 cm^3 g_{cat}^{-1} h^{-1}. A permanent gas detection prior to reaction was used to perform raw gas analysis under high-pressure conditions for consistent data evaluation for at least 5 h. Afterwards, the catalyst was heated with 5 °C min^{-1} to 160 °C and slowly with 0.06 °C min^{-1} to 260 °C. The catalyst was measured under isothermal conditions for 72 h to exclude medium-term aging effects.

After the induction period, the reaction temperature, the residence time, the total pressure and the partial pressures of H_2 and CO were successively varied. Each parameter step was held for at least 8 h to assure steady-state conditions. After the temperature variation had been performed, a fresh catalyst was used for the other variations. The conditions for these variations are summarized in Table 1. The temperature variation was performed as a stepwise increase from 260 °C

Table 1 Conditions for the temperature, total pressure and residence time variation

Varied parameter	GHSV/cm^3 g_{cat}^{-1} h^{-1}	p/bar	T/°C
GHSV	6000, 12 000, 24 000	60	260
p	12 000	20, 40, 60	260
T	12 000	60	260–280

Table 2 Applied partial pressure variation

Step	$p(CO)$/bar	$p(H_2)$/bar	$p(N_2)$/bar	H_2/CO
1	24	24	12	1.0
2	**18**	24	18	1.3
3	**15**	24	21	1.6
4	**12**	24	24	2.0
5	**9**	24	27	2.7
6	24	24	12	1.0
7	24	**19**	17	0.8
8	24	**17**	19	0.7
9	24	**15**	21	0.6
10	24	**12**	24	0.5
11	24	24	12	1.0

to 280 °C in steps of 5 °C, followed by a decrease to 260 °C without further steps.

The applied partial pressures are summarized in Table 2. The first part of the variation varied the CO partial pressure, while the next part included a lowering of the H$_2$ partial pressure. To maintain the constant pressure of 60 bar, the partial pressure of N$_2$ was adjusted correspondingly. After each variation, the initial reaction conditions were applied to study the influence of the respective variation on the catalyst.

Additionally, ethylene co-feeding experiments were performed with a fresh catalyst. After reaching steady state, a constant gas flow of ethylene was added to the feed, which was varied in steps of 2.5 vol% up to 10 vol%. To maintain a constant H$_2$/CO ratio, the GHSV was increased to 24 000 cm^3 g$_{cat}^{-1}$ h^{-1} and the volume flow of N$_2$ was lowered to compensate for the presence of ethylene in the feed.

Following the ethylene co-feeding experiments, a fresh catalyst was used to further investigate the presence of an anchored molecular Co-based active site. For that purpose, the cold trap attached to the exhaust line of the setup was filled with 2-propanol (2-PrOH), set to 0 °C, and switched online after reaching the reaction temperature of 260 °C. The collection time of approx. 190 h time on stream (TOS) conducted under isothermal conditions consisted of a short induction period under the initial reaction conditions followed by cycling the GHSV from 6000 cm^3 g$_{cat}^{-1}$ h^{-1} over 12 000 cm^3 g$_{cat}^{-1}$ h^{-1} to 24 000 cm^3 g$_{cat}^{-1}$ h^{-1} with each step being held for 8 h TOS. The collected liquid was analysed by inductively coupled plasma mass spectrometry (ICP-MS) using a Thermo Scientific iCAP RQ ICP-MS instrument equipped with a kinetic energy discrimination cell and a quadrupole MS. The sample was placed in a polytetrafluoroethylene liner and diluted to the desired concentrations.

Data evaluation was performed by using 2-D online GC optimized for the separation of alcohols and hydrocarbons as well as the separation of paraffins and olefins within the hydrocarbon distribution. A detailed insight into the analysis is given in the SI part. Volume contraction during HAS, which results in changed molar fractions of products in the effluent gas stream, was compensated by an inert standard.

Additionally, a power-law model was used to determine the reaction orders m and n based on the independent variation of $p(CO)$ and $p(H_2)$. Eqn (14) shows the applied rate law with the reaction rate r and the reaction rate constant k. The influence of the products was neglected while applying this model.

$$r = k \cdot p(CO)^m \cdot p(H_2)^n \tag{14}$$

To determine the reaction orders, the linearized form of eqn (14) was used.

$$\ln(r) = \ln(k') + m \cdot \ln(p(CO)) \text{ with } p(H_2) = \text{const} \tag{15}$$

$$\ln(r) = \ln(k'') + n \cdot \ln(p(H_2)) \text{ with } p(CO) = \text{const} \tag{16}$$

Transient kinetics

The pulse experiments were performed in a setup built for transient measurements,[39] which consisted of a 1/4″ fixed-bed stainless steel reactor equipped with an axial thermocouple in the middle of the catalyst bed. The reactor tube with an inner diameter of 4.5 mm was additionally coated with SilcoNert2000®. The coated reactor was placed inside of a single-zone furnace to establish a 5 cm long isothermal zone. 200 mg of the Mn$_1$Co$_{11}$ catalyst with a sieve fraction of 250–355 μm were placed inside the reactor and heated according to our established treatment.[7,8] High-pressure pulses of 1 mL with a defined molar amount of the specific probe molecule were introduced into the syngas feed flow. The high-pressure pulse unit consisted of one 6-port-2-position dosing valve equipped with a 1 mL sample loop and two identical back pressure regulators (BPR) coupled with one process pressure controller. One BPR was integrated in the reactor line between the reactor outlet and the analytics, while the other one was positioned in the pulse line between the sample loop and the exhaust. Switching the 6-port-2-position valve thereby resulted in the injection of a pulse into the syngas stream without a pressure drop.[39] A high-pressure evaporator system supplied by Bronkhorst Deutschland Nord GmbH enabled high-pressure pulse experiments using chemicals with high boiling points that are not available in a sufficient concentration in gas cylinders.[41]

The effluent was analysed using a Nicolet is50 FTIR spectrometer equipped with a transmission gas cell, allowing a time resolution of one spectrum every 30 s. The gas cell consisted of a stainless-steel cylinder with a pathlength of 150 mm and an inner cell diameter of 10 mm resulting in a volume of 7.5 mL. The inner walls of the gas cell were coated with gold. To investigate the effects of the applied pulses, this study focused on the analysis of the effects on the mole fractions of CO$_2$, H$_2$O, the linear alcohols MeOH, EtOH, 1-propanol (1-PrOH) and 1-butanol (1-BuOH) as well as on the hydrocarbons methane, ethane and ethylene, which were the products with the highest molar amounts in the product gas stream. Furthermore, in addition to our previous study on transient kinetics over the 2CoCu catalyst,[11] the key

Table 3 Mole fractions of the probe molecules pulsed into the gas feed. Each component (CO_2, CO, H_2 and MeOH) was diluted with N_2 to establish the desired mole fraction and was pulsed separately

	Pulse series		
Gas	1	2	3
CO/vol%	0	30	70
H_2/vol%	10	55	90
CO_2/vol%	0.0	3.0	8.0
MeOH/vol%	0.35	0.46	0.88

intermediates acetic acid, propionaldehyde, and acetaldehyde were calibrated and monitored as well.

To achieve the desired GHSV of 12 000 cm^3 g_{cat}^{-1} h^{-1}, the syngas flow with a $H_2:CO$ ratio of 1 ($H_2:CO:N_2 = 40:40:20$) was adjusted to 40 cm^3 min^{-1}. After the induction period of 100 h at 260 °C and a pressure of 60 bar, the pulse series were started. While the syngas flow with a $H_2/CO = 1$ ratio was maintained through the reactor line, the desired mole fraction of the probe molecule was flushed through the pulse line including the sample loop. With both lines showing an identical pressure, the 6-port-2-position dosing valve was switched resulting in the volume of the sample loop to be injected to the reactor line. After the probe molecule had been completely removed from the sample loop, the valve was switched again allowing the sample loop to be flushed with the desired molar amount of probe molecule for the next pulse. The performed pulse experiments are summarized in Table 3.

Results

In situ DRIFTS

In situ DRIFTS measurements were conducted during the heating phase in syngas. Fig. 1 shows the obtained spectra in the range from 800 to 1900 cm^{-1}, and the full range is shown in Fig. S1.
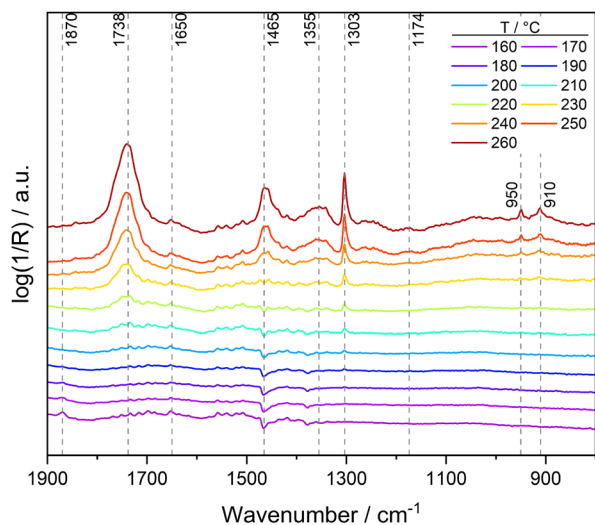

Fig. 1 DRIFT spectra obtained during the heating phase in 20 cm^3 min^{-1} syngas with a H_2/CO ratio of 1 and a pressure of 60 bar.
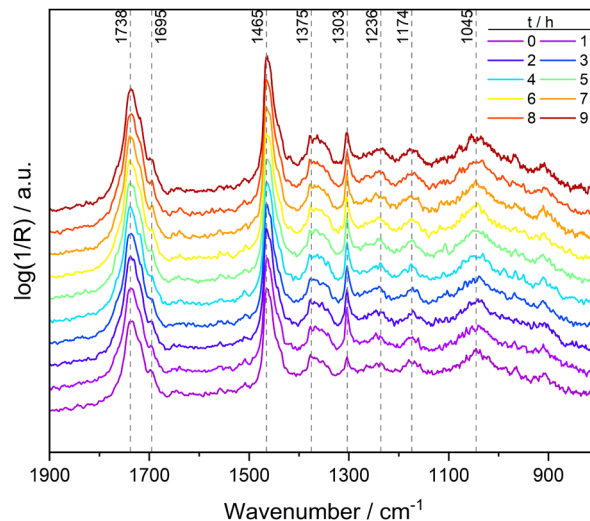

Fig. 2 DRIFT spectra obtained during the induction period at a temperature of 260 °C, a H_2/CO ratio of 1, 20 cm^3 min^{-1} syngas and a pressure of 60 bar.

The obtained spectra clearly show that bands resulting from products start to appear after reaching a temperature of 210 °C, whereas a small band at 1870 cm^{-1} is visible at a temperature of 160 °C, which can be assigned to Co mononitrosyl species.[42] The observed product bands increased strongly at higher temperature due to increasing CO conversion. Additionally, a band at 2349 cm^{-1} was observed indicating CO_2 formation.[43] Due to the applied total pressure of 60 bar using undiluted syngas, the intensity of the CO band exceeded the detector limit. Therefore, an analysis of this spectral range was not possible.

After the heating phase, the induction period was monitored as well. Fig. S2 shows the full spectral range, while Fig. 2 focuses on the low frequency area, and Fig. S3 shows a higher resolution of the v(C–H) area. Table 4 summarizes the observed bands and their assignments during the heating

Table 4 Observed IR bands and their assignment during the heating phase and induction period of the Mn_1Co_{11} catalyst using 20 cm^3 min^{-1} syngas with a H_2/CO ratio of 1 and a pressure of 60 bar

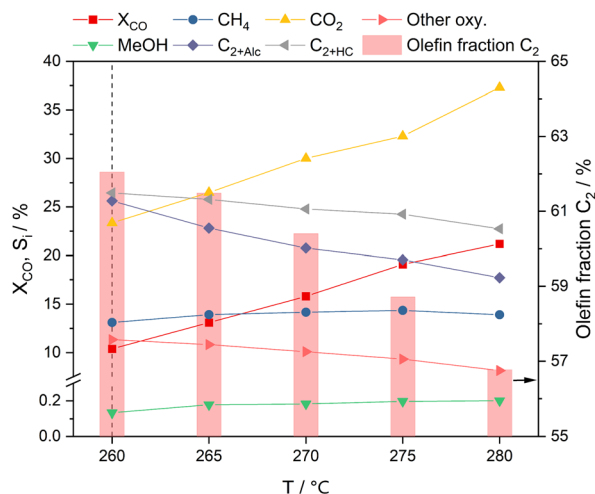| IR band per cm^{-1}	Assignment	Product
1738	v(C=O)	aldehydes[43,44]
2711	v(O–H)	acids[44]
1695	v(C=O)	
1355	C–O–H deformation	alcohols[44]
1174	v(C–O)	
1045	v(C–O)	
1236	v(C–O–C)	ethers[44]
2956	$-CH_3$ v_s(C–H)	alkanes[43,44]
2930	$-CH_2-$ v_{as}(C–H)	
2871	$-CH_3$ v_{as}(C–H)	
2854	$-CH_2-$ v_s(C–H)	
1465	$-CH_3$ δ_{as}(C–H)	
1375	$-CH_3$ δ_s(C–H)	
3014	v(C–H)	methane[45]
1303	δ(CH_4)	

Fig. 3 Summarized selectivities and CO conversion as a function of temperature. The C$_2$ olefin fraction is shown as a bar diagram. The standard reaction conditions are marked with a dashed line.

phase as well as the induction period. The formed products comprise aldehydes, acids, alcohols, ethers, alkanes and methane.

Steady-state kinetics

After reaching steady state, the parameter variations were conducted. The first experiment was the temperature variation described in the experimental section, followed by residence time and partial pressure variations as well as the co-feeding of ethylene. A summary of the absolute pressure variation is given in the SI part. Fig. 3 shows the summarized selectivities as well as CO conversion as a function of temperature. Furthermore, the results are summarised in Table S1.

Fig. 3 shows that CO conversion increased approximately linearly with increasing temperature. Starting from 10.4% at 260 °C, a conversion of 21.2% was reached at 280 °C. A similar trend was observed for the CO$_2$ selectivity, which increased from 23.4% to 37.3% at 280 °C. In contrast to the CO$_2$ selectivity, the selectivities of the C$_{2+HC}$ and C$_{2+Alc}$ fractions decreased with increasing temperature. Starting with 26.4% for C$_{2+HC}$ and 25.6% for C$_{2+Alc}$, a higher temperature led to a linear decrease reaching selectivities of 22.7% and 17.7% at 280 °C for C$_{2+HC}$ and C$_{2+Alc}$, respectively. A comparison of these values illustrates that the decrease of the long-chain hydrocarbons was less pronounced compared with the selectivities of the long-chain alcohols. However, as the detailed comparison of the primary and secondary alcohols in Fig. S5a and b indicates, respectively, only the primary and secondary C$_{4+Alc}$ selectivities decreased with increasing temperature, while the EtOH and 1-PrOH selectivities increased. Slight increases at higher temperatures were observed for the MeOH and the CH$_4$ selectivity. The selectivities of all other oxygenates (oxy.) consisting mainly of acetaldehyde as well as acetic acid,

propionaldehyde and low amounts of dimethyl ether (DME) and diethyl ether (DEE), decreased with increasing temperature, which is shown in detail in Fig. S5c. Furthermore, since the customized GC application allowed further insight into the olefin fraction of the C$_2$–C$_6$ fractions, Fig. 3 shows that the olefinicity of the C$_{2HC}$ fraction slightly decreased with increasing temperature. Thus, the product distribution was severely influenced by the higher temperature, pointing to structural transformations of the catalyst.[7,8] These structural transformations also led to changes in CO conversion and selectivity when cooling to 260 °C after the temperature increase to 280 °C, which is shown in Fig. S6 in comparison to the corresponding values at 260 °C before the temperature variation. After the temperature variation, CO conversion decreased to 8.8%, which is significantly lower compared with the value prior to heating. The CO$_2$ and C$_{2+HC}$ selectivities slightly decreased, while the other oxygenates increased in selectivity. The CH$_4$, MeOH, and C$_{2+Alc}$ selectivities were not significantly influenced. Additionally, the apparent activation energy was derived using the Arrhenius equation. The linearization (Fig. S4) resulted in an apparent activation energy of 88 kJ mol^{-1}. This value is significantly lower compared with the previously investigated 2CoCu catalyst, for which an activation energy of 140 kJ mol^{-1} was derived.[5]

Due to the observed deactivation of the catalyst during the temperature variation, a new catalyst sample was used for the remaining parameter variation. After reaching steady state and a CO conversion of 8.6%, the residence time was varied first. The summarized selectivities as well as CO conversion are shown in Fig. 4 and summarised in Table S2.

As expected, CO conversion is strongly influenced by the GHSV. Doubling the GHSV resulted in a value of 4.7%, while halving the GHSV led to a CO conversion of 16.5%. This dependence of CO conversion indicates that the influence of
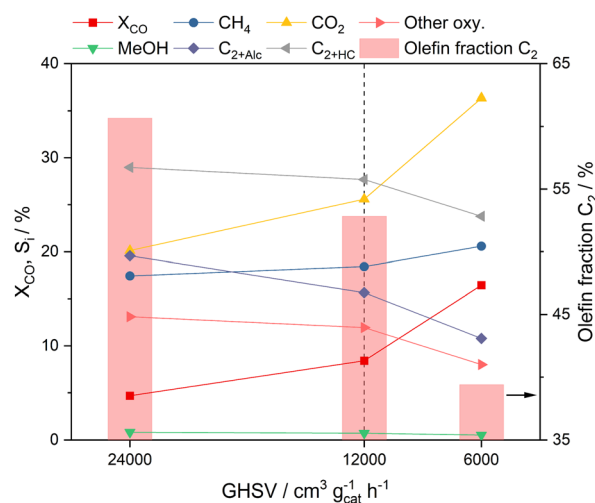

Fig. 4 Summarized selectivities and CO conversion as a function of GHSV. The C$_2$ olefin fraction is shown as a bar diagram. The standard reaction conditions are marked with a dashed line.

the formed products on the HAS rate is negligible under the chosen reaction conditions. Increasing the GHSV decreased the CO_2 selectivity to 20.1%, while a lower GHSV resulted in an increase up to 36.3%. Interestingly, CO conversion and CO_2 selectivity have the same trend as a function of GHSV, which seems to be closely linked to water formation and the WGSR.

A reversed trend was observed for the C_{2+Alc} and C_{2+HC} selectivities. A more detailed comparison of the selectivities of the primary and secondary alcohols as well as other oxygenates is shown in Fig. S7. While the increasing C_{2+Alc} selectivity with higher GHSV can be contributed to the higher selectivities of the primary and especially secondary C_{4+Alc} fraction, the selectivities of EtOH and 1-PrOH decreased slightly. In comparison, the secondary alcohols, with the exception of 2-PrOH, increased with increasing GHSV. The selectivities of all other oxygenates decreased significantly with lower GHSV.

Compared with the 2CoCu catalyst, for which an increase of the GHSV led to a decrease in C_{2+HC} selectivity, the trend was reversed using the Mn_1Co_{11} catalyst while the selectivities for the other product groups as well as CO conversion showed similar trends. However, the influence of GHSV on the C_{2+Alc} selectivity was more pronounced for the PBA-based catalyst. This can be mainly assigned to the strong increase in secondary alcohol formation with increasing GHSV, since this product group was not reported for the 2CoCu catalyst.[5]

Following the total pressure variation, which is described in the SI part, the partial pressures of H_2 and CO were varied according to Table 1. The obtained summarized selectivities as well as CO conversion for each step are shown in Fig. 5 and in Table S3.

The H_2/CO ratio was at first increased up to a value of 2.7 resulting in a linear CO conversion increase up to 34.2%, whereas decreasing the H_2/CO ratio below 1.0 resulted in a

diminished CO conversion down to 5.4%. An increasing CO_2 selectivity was observed both with decreasing and increasing H_2/CO ratio. The highest selectivities during both partial pressure variations were obtained with the H_2/CO ratio which differed the most from the standard conditions. Increasing the H_2/CO ratio above 1.0 resulted in a slight decrease of the C_{2+Alc} selectivity from 16.8% to 15.2%, while the C_{2+HC} selectivity decreased more strongly from 25.9 to 19.1%. The most significant decrease in selectivity was observed for the other oxygenates, which decreased from 10.6 to 2.6% as shown in detail in Fig. S10c. Both the C_{2+Alc} and the C_{2+HC} selectivities decreased stepwise when decreasing the H_2/CO ratio from 1.0 to 0.8, while a slight increase was observed for the other oxygenates. However, decreasing the ratio further did not result in significant changes regarding the C_{2+Alc} and other oxygenate selectivities, while the C_{2+HC} selectivity increased up to 26.8%.

In contrast, the MeOH and methane selectivities behaved differently. Due to the higher H_2 partial pressure, a methane selectivity of 24.0% was reached at a H_2/CO ratio of 2.7, while MeOH was not significantly influenced by the change in H_2/CO ratio, thereby remaining at values between 0.5 and 0.7%. This is a noticeable contrast to the 2CoCu catalyst, where an increase of the H_2/CO ratio led to significant increases in MeOH selectivity.[5] This trend was reversed when applying H_2/CO ratios below 1.0. While the MeOH selectivity was not influenced again, the methane selectivity decreased strongly from 16.4% to 11.6%. Additionally, a strong dependence of the C_2 olefinicity on the H_2 partial pressure was observed resulting in a strong decrease of the olefinicity with increasing H_2/CO ratio. Fig. S10 shows the selectivities of the analyzed primary and secondary alcohols in more detail. Interestingly, the rather stable C_{2+Alc} selectivity at H_2/CO > 1.0 can be attributed mostly to the increasing EtOH selectivity. Additionally, higher 1-PrOH and 1-BuOH selectivities were observed as well, while the MeOH and C_{5+Alc} selectivities were not significantly influenced when increasing the H_2/CO ratio to 2.7. A pronounced decrease was observed in Fig. S10b for the secondary alcohols. The opposite was observed at H_2/CO < 1.0, since the selectivities of all primary C_{3+Alc} and especially EtOH decreased while significant increases in secondary C_{3+Alc} selectivities were observed, therefore leading to an overall slight increase of the C_{2+Alc} selectivity at low H_2/CO ratios. Thus, the varied partial pressures influenced the product distribution strongly. However, the comparison at H_2/CO = 1.0 before and after the individual partial pressure variations shown in Fig. S11 indicates that the changing partial pressures induce structural transformations which are not fully reversible, thereby leading to noticeable selectivity changes, which may have superimposed the selectivity changes induced by the partial pressure variations. The XRD pattern of the sample used for the steady-state kinetic investigations including the residence time, absolute pressure, and partial pressure variations is shown in Fig. S19d. Compared with the previously reported Co_2C crystallite size of 19.3 nm after the induction period,[8] an increased crystallite size of 20.5 nm was derived. In addition, more intense $MnCO_3$ reflections
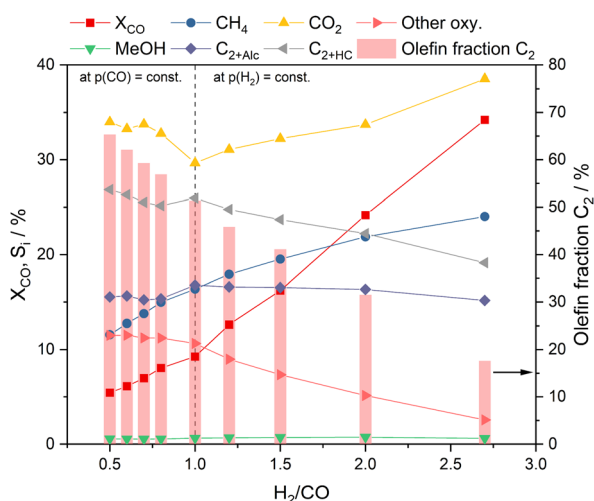

Fig. 5 Summarized selectivities and CO conversions as a function of the H_2/CO ratio. The C_2 olefin fraction is shown as a bar diagram. The standard reaction conditions are marked with a dashed line.

were observed after the extended TOS and the parameter variations. Further structural analysis of the Mn_1Co_{11} catalyst, which was in the focus of our previous publication,[8] is provided in the SI part.

Based on the performed partial pressure variations, a power-law model was applied to derive the reaction orders. The linearized plots of both variations are shown in Fig. 6. While a reaction order of 0.7 was calculated for H_2, a negative value of approx. −0.3 was obtained for CO, indicating a slight inhibition by CO. While the reaction order for H_2 is similar to the value of 0.8 derived for the 2CoCu catalyst, no inhibition by CO was observed for 2CoCu according to its reaction order of 0.[5]

To further study the interplay of the carbonylation of primary alcohols and the reductive hydroformylation, ethylene co-feeding experiments were performed. The obtained chromatograms as well as the quantitative analysis are shown in Fig. 7. While an increasing molar fraction of ethane, propionaldehyde and 1-PrOH was expected, Fig. 7a shows clearly that no other primary alcohol increased as indicated by the 1-BuOH peaks. Additionally, Fig. 7b shows that propionaldehyde as well as 1-PrOH increased strongly and linearly with respect to the higher molar amount of ethylene co-fed under reaction conditions. While the thereby calculated increase in GC peak area is shown in Fig. S15 and 7c compares the derived mole fractions of ethane, propionaldehyde and 1-PrOH as a function of the co-fed ethylene, demonstrating a significant linear increase with increasing molar amount of co-fed ethylene due to the hydroformylation of ethylene to propionaldehyde and its subsequent hydrogenation to propanol. The trend observed for ethane clearly differed, because surpassing a molar amount of 7.5 vol% ethylene did not result in a further increase of ethane. Thus, co-feeding of ethylene revealed that the reductive hydroformylation occurred independently from the reductive carbonylation of primary alcohols, suggesting two different active sites.
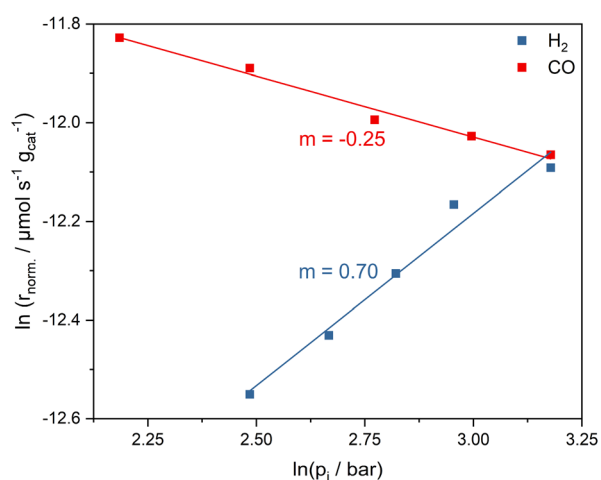

Fig. 6 Linearized plots of the logarithmic reaction rate *r* as a function of the CO and H_2 partial pressures and the derived reaction orders for CO and H_2.
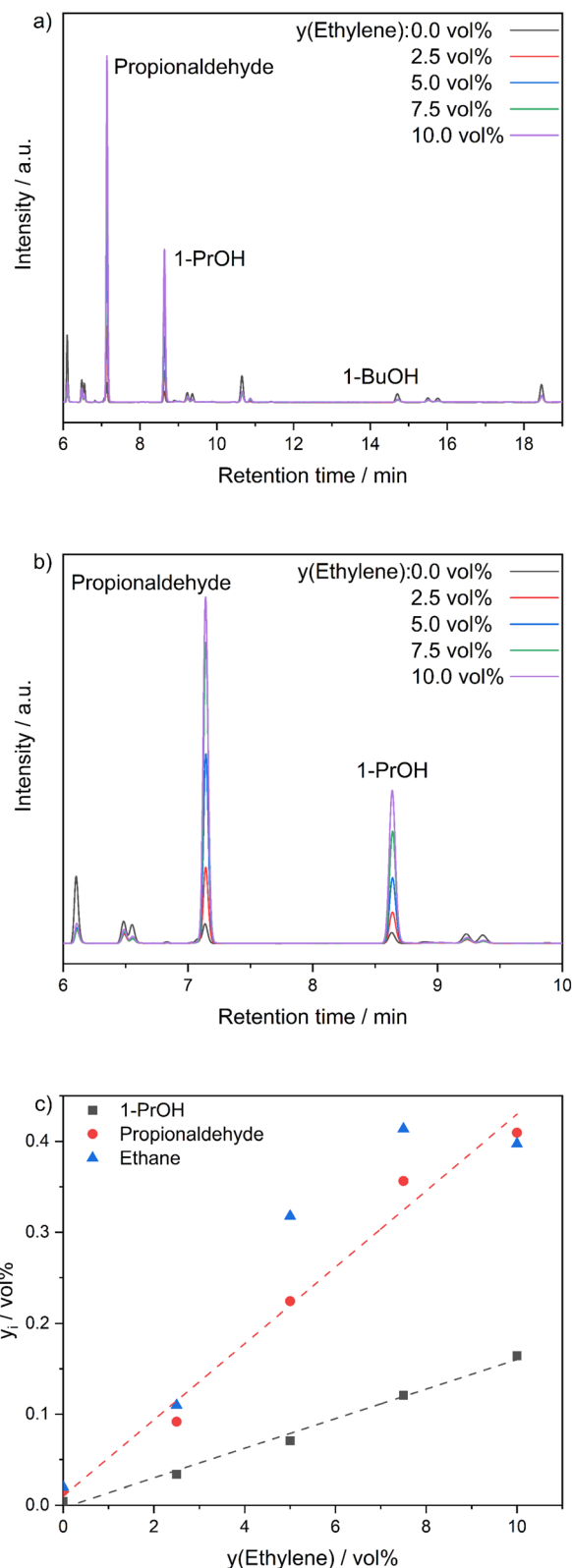

Fig. 7 a) Chromatograms recorded during the ethylene co-feeding series, b) enlarged peaks of propionaldehyde and 1-PrOH, and c) the calculated mole fractions of 1-PrOH, propionaldehyde and ethane as a function of co-fed ethylene.

The presence of the Co–N–C sites anchored by the functionalized carbon matrix was additionally investigated by analysing the product gas stream collected in the cold trap during a kinetic measurement using a fresh sample while varying the GHSV. The performed ICP-MS analysis of the 2-PrOH solution showed a Co mass concentration of 3.5 mg L^{-1} being present after 190 h TOS, thus confirming the presence of a volatile molecular Co species.

Transient kinetics

To further study the proposed reaction network for HAS over the Mn_1Co_{11} catalyst, high-pressure pulse experiments were performed. Similar to our previous investigation of the transient kinetics over the 2CoCu catalyst,[11] the influence of the probe molecules CO, H_2 and CO_2 on the product distribution was investigated. These pulse series are shortly summarized in the SI part showing that CO_2 does not disturb the alcohol formation. The H_2 and CO pulse series confirmed the results of the partial pressure variations.

Furthermore, to gain further insight into the interplaying mechanisms, high-pressure MeOH pulses were performed. Fig. 8a shows the effect of the performed MeOH pulses on the mole fractions of the C_1–C_4 alcohols. Injecting the 0.35 vol% MeOH pulse as the pulse with the lowest amount of MeOH already resulted in a clear increase in all monitored alcohols.

While this increase was rather moderate for 1-PrOH, the mole fractions of EtOH and 1-BuOH increased significantly even with the lowest molar content of MeOH in the pulse. By further increasing the molar fraction of MeOH in the pulse up to 0.88 vol%, this increase became even more pronounced resulting in more than doubled mole fractions of long-chain alcohols over a short period of time indicating the fast reductive carbonylation of MeOH to short-chain alcohols.

Fig. 8b shows the mole fraction of the investigated hydrocarbons during the MeOH pulse series. While the molar amounts of methane and ethylene were clearly diluted due to the performed pulses, this effect was less pronounced for ethane. Except for the dilution effect, no further impact on the formation of hydrocarbons was observed. Fig. 8c shows a similar effect on the mole fractions of CO and H_2O. Furthermore, Fig. 8d displays the mole fractions of acetaldehyde, propionaldehyde and acetic acid during the performed MeOH pulse series, which also experienced the mentioned dilution effect. Only the performed MeOH pulse with 0.88 vol% resulted in a deviation of this trend for acetic acid, but no clear increase was observed.

Discussion

The observed accelerated formation of primary alcohols due to pulsed MeOH (Fig. 8) shows that the carbonylation of primary
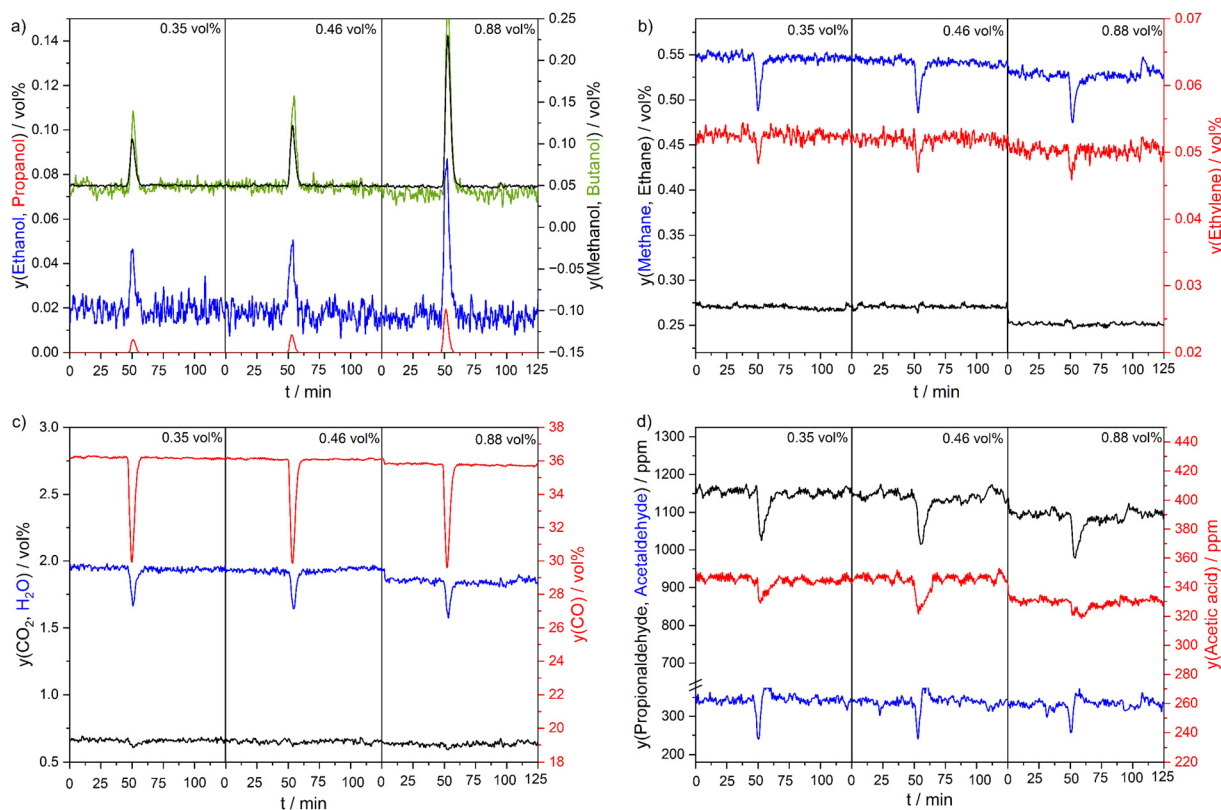

Fig. 8 Recorded mole fractions of a) the linear C_1–C_4 alcohols, b) methane, ethane and ethylene, c) CO, CO_2 and H_2O and d) acetaldehyde, acetic acid and propionaldehyde during the MeOH pulse series. The mole fractions of the dosed MeOH pulses are shown above the pulses.

alcohols, as proposed in our previous work,[7,8] is indeed taking place and is the main factor regarding the oxygenate formation using PBA-derived catalysts, as demonstrated by the significant increase of the molar fraction of 1-BuOH. Furthermore, the fast carbonylation pathway offers an explanation for the MeOH selectivity observed during all performed experiments which is surprisingly low compared with the MeOH selectivity of the 2CoCu catalyst[5] and all other primary alcohols formed over the Mn_1Co_{11}. Most MeOH seems to be directly consumed resulting in the formation of more primary C_{2+Alc} as well as the intermediate oxygenates such as acetic acid and acetaldehyde. Additionally, the parameters investigated in this study do not seem to significantly influence the rate of this initial step of the carbonylation pathway.

The pulse experiments can be compared to the co-feeding of ethylene described earlier, which was performed to investigate the influence of the hydroformylation-hydrogenation tandem reaction. While co-feeding resulted in significant increases of 1-PrOH and propionaldehyde, this was not observed for 1-BuOH or higher oxygenates. In comparison, even though the performed high-pressure pulses contained up to 0.88 vol% MeOH, which is a significantly lower volume fraction than the added ethylene, an effect of MeOH on the chain growth to long-chain alcohols was observed. Therefore, the combination of both measurements clearly demonstrates that the reductive hydroformylation and carbonylation of primary alcohols are catalysed by two different Co-based active sites and that both reactions need to be analysed independently from each other when investigating PBA-derived catalysts. It was recently reported that a Co catalyst obtained by the pyrolysis of the metal–organic framework (MOF) ZIF-67 is active for reductive hydroformylation.[46] While the study focused on the hydroformylation of liquid olefins, the MOF-derived catalyst featured various structural similarities with the PBA-based Mn_1-Co_{11}, i.e., a N-doped carbon matrix with embedded Co nanoparticles.[46] In addition to the known Co_2C/Co^0 interface sites, it must be assumed that the other active site is closely linked to the carbon matrix. Thus, we have previously proposed the presence of additional Co–N–C sites.[7,8]

Overall, the carbonylation of the primary alcohol to the corresponding long-chain carboxylic acid and the hydroformylation step from the olefin to the aldehyde are key steps for CO hydrogenation to higher alcohols but differ in their results. Due to carbonylation, the corresponding carboxylic acid is formed first and during its hydrogenation to the primary alcohol, the corresponding aldehyde is formed as an intermediate, so that the acid is overall formed to a much lower extent compared with the aldehyde which is additionally obtained via the hydroformylation of olefins.[7,8]

Even though the formation of the C_2–C_4 alcohols was accelerated as observed in Fig. 8a, the dilution of the mole fraction of water prevails. This is ascribed to the dilution effect observed for the hydrocarbons. While this effect is only visible for the C_1 and C_2 fractions, it must be assumed that a similar effect was influencing the higher hydrocarbon fractions which were observed in the investigations applying

GC analysis but cannot be satisfactorily distinguished from the C_1 and C_2 fraction by FTIR spectroscopy. Interestingly, no response of CO_2 was observed. Similar to our previous study,[11] this is a clear indication that a network of several slow solid-state reactions resulted in the observed CO_2 formation involving the formation and decomposition of Co_2C.[7,8,11] Similar to the components shown in Fig. 8b and c, a dilution effect on the mole fractions of acetaldehyde, propionaldehyde and acetic acid was observed for every performed pulse. This was rather unexpected, especially regarding acetic acid. Due to the observed acceleration of the carbonylation reaction pathway, an excess of MeOH was expected to result in a higher mole fraction of carboxylic acids. These acids are in turn hydrogenated, which resulted in the observed acceleration of the formation of the long-chain alcohols. Therefore, it must be assumed that the hydrogenation rate to the alcohol is considerably higher than the carbonylation rate to the carboxylic acid. This is further supported by analysing the molar amount of acetic acid during the performed pulses. Increasing the amount of MeOH in the pulse up to 0.88 vol% resulted in a slightly less pronounced dilution effect, which could indicate that a certain threshold of MeOH is necessary for the accumulation of acetic acid to occur, which was not possible to be surpassed using the performed MeOH pulses.

The obtained in situ DRIFT spectra showed the presence of a band at 1870 cm^{-1} with low intensity at 160 °C. Since chromatograms obtained at this temperature demonstrated the absence of product formation, it must be concluded that this band results from a structural rearrangement. It is known in literature that metal mononitrosyls with rather weak M–N bonds can be identified by bands in this region.[42] In our past study, elemental analysis of the catalyst revealed a high degree of N- and O-functionalization.[7,8] Therefore, it is assumed that the syngas atmosphere resulted in structural transformations of the carbon matrix at low temperatures leading to the release of NO, which weakly binds to the present Co metal atoms, finally resulting in a replacement of NO by CO at higher temperatures.

Reaching a temperature of 260 °C, the observed bands mostly had high intensities allowing a clear assignment. The bands shown in Fig. 2 demonstrate the formation of aldehydes ($v(C{=}O)$), acids ($v(C{=}O)$), and alcohols ($v(C{-}O)$). Even though past studies showed that aldehydes and especially acids have rather low selectivities compared with the total alcohol selectivity,[7,8] the spectra provide evidence for the reductive hydroformylation and carbonylation pathways over the PBA-derived catalyst.

The temperature variation was part of the steady-state kinetic investigations. When comparing CO conversion and selectivities before and after the temperature variation, deactivation of the catalyst was identified, which is most likely associated with sintering. In our past study, we thoroughly characterized the washed catalyst in the different states and observed an increase of the Co_2C crystallite size compared with the unwashed K-promoted catalyst. Furthermore, TEM images after HAS

revealed a particle size distribution reaching slightly higher values.[7,8] In good agreement with past observations, the C_2 olefin fraction decreased with increasing temperatures.[7,8] Interestingly, the olefinicity at 260 °C after performing the temperature variation was higher compared with the initial value. Therefore, sintering resulted in a diminished rate of hydrogenation, which is in accordance with the slightly lower CH_4 selectivity. Since the alcohol selectivities did not decrease after reaching the temperature of 260 °C again, sintering had a stronger impact on the Co^0 sites than on the Co_2C/Co^0 interface sites and the molecular Co sites.

The derived apparent activation energy of 88 kJ mol^{-1} was clearly lower than the apparent activation energy of 140 kJ mol^{-1} of the 2CoCu catalyst.[5] Consequently, significantly higher degrees of CO conversion were achieved over the Mn_1Co_{11} catalyst throughout all parameter variations. This further underlines the potential of the PBA-derived catalysts to be utilized at lower temperatures, which will be an essential aspect of future studies.

The CO_2 selectivities observed during the GHSV variation can be attributed mainly to the influence of the WGSR. Furthermore, the changing coverages of adsorbed CO and atomic hydrogen must be considered. According to Göbel et al.,[5] the coverage of the surface intermediates and CO_{ads} reached lower values with higher CO conversion for the 2CoCu catalyst. Thus, a higher coverage of adsorbed hydrogen was obtained resulting in a higher hydrogenation rate. This was demonstrated by the decrease in olefin fractions, especially of the C_2 hydrocarbon fraction, as well as a decrease in C_{2+Alc} selectivity, since the CO insertion according to the carbide-based mechanism requires a high coverage of CO. Consequently, a lower conversion led to an inversed trend resulting in a diminished influence on the hydrogenation of the surface growth intermediates due to a low coverage of H_{ads} which led to an increase of the alcohol selectivities.[5] Since lowering the GHSV resulted in a drastic decrease of the C_2 olefinicity to 39%, while it increased up to 61% for a higher GHSV, it can be assumed that the rate of hydrogenation over the Mn_1Co_{11} catalyst corresponds to that of the 2CoCu catalyst. This is further supported by the shift to short chain lengths with lower GHSV for hydrocarbons as well as primary alcohols due to a faster interruption of the chain growth on the catalyst surface according to the carbide-based mechanism. In addition, the significant decrease of the selectivities for other oxygenates comprising mainly acetaldehyde, propionaldehyde, and acetic acid shows that the influence of hydroformylation as well as of carbonylation is diminished at low GHSV and correspondingly high CO conversion due to the reduced availability of CO.

To further verify this assumed dependence on conversion and surface coverage, the summarized selectivities were plotted as a function of conversion, which is shown in Fig. S8. The linear trends in this plot suggest that the observed selectivities can indeed be clearly described as a function of CO conversion. At higher conversion, the selectivities of CO_2, especially, as well as of methane increased strongly, while the other products decreased.

Interestingly, the alcohol selectivities displayed in detail in Fig. S7 show that the observed increase of long-chain alcohols with higher GHSV can be attributed to the increasing selectivity of the C_{4+} primary and especially secondary alcohols, while EtOH and 1-PrOH had a slightly decreased selectivity. Furthermore, the selectivities regarding other oxygenates increased slightly. Taking the proposed intertwined reaction network into consideration, the high GHSV and correspondingly low CO conversion resulted in an increased availability of CO, which led to an acceleration of the carbonylation pathway, thereby consuming short-chain alcohols and leading to the formation of long-chain alcohols as well as of aldehydes and acids as intermediates. The thereby increased acidity in conjunction with the significantly increased olefin fractions at high GHSV also explains the increase in secondary alcohol selectivity, which were previously proposed to be obtained by hydration of the corresponding olefins.[7,8]

Despite the previously discussed differences regarding reaction mechanisms and active sites, the global reaction order for H_2 derived for the PBA-based catalyst is similar to other systems such as the 2CoCu catalyst, but the value derived for CO indicates a slight inhibition in contrast to the 2CoCu catalyst.[5] The correspondingly changing CO conversion during the partial pressure variations can be directly linked to the impact of the surface coverages of adsorbed hydrogen and CO. By increasing H_{ads}, methane formation is favoured resulting in high CO conversion. In contrast, lowering the H_2/CO ratio below 1.0 resulted in an inhibited hydrogenation of the C_1 species on the surface. This becomes obvious by comparing the methane selectivity with the selectivity of the long-chain hydrocarbons shown in Fig. 5: while the methane selectivity constantly decreased to 11.6%, the C_{2+HC} value increased up to 26.8%.

A higher H_2/CO ratio resulted in a slight decrease in C_{2+Alc} selectivity down to 15.2%, while H_2/CO ratios below 1.0 did not result in significant selectivity changes. Overall, this behaviour seems to be similar to the 2CoCu catalyst,[5] but a more detailed comparison reveals various differences. The decrease in C_{2+Alc} selectivity with increasing H_2/CO ratio for the 2CoCu catalyst was the result of decreasing selectivities for all primary C_{2+Alc}.[5] However, the overall decrease in C_{2+Alc} selectivity for the Mn_1Co_{11} catalyst was due to decreasing secondary alcohol selectivities, while the formation of primary C_{2+Alc} increased, which was especially significant for EtOH, 1-PrOH, and 1-BuOH. Taking also the significant selectivity decrease regarding the other oxygenates into account, these trends highlight the mechanistic differences between both types of catalyst. While for the 2CoCu catalyst, an increase of the H_2/CO ratio results in less CO insertion into the carbon chains growing on the catalyst surface according to the carbide-based mechanism, for the Mn_1Co_{11} catalyst the surplus in H_2 results in a faster hydrogenation of the intermediates obtained by hydroformylation and carbonylation, which thereby results in the formation of more long-chain primary alcohols.

Comparing the product distribution under standard reaction conditions after both partial pressure variations (Fig. S11), it becomes obvious that the deviating H_2/CO ratio influenced the overall product distribution permanently. Notably, changes in CO_2, C_{2+HC}, and C_{2+Alc} selectivities were observed once the H_2/CO ratio exceeded 1.0. The decrease in C_{2+Alc} selectivity can primarily be attributed to a reduced formation of secondary alcohols and primary C_2–C_4 alcohols, while slight increases were observed for 1-PeOH and 1-HexOH. These findings suggest that the increased H_2/CO ratio caused a permanent modification of the carbon matrix, which in turn affected all active sites of the Mn_1Co_{11} catalyst.

Even when reaching a value of 0.5 for the H_2/CO ratio, corresponding to a significantly higher CO partial pressure, it was not possible to fully regenerate the Mn_1Co_{11} catalyst. Since most of the products reached the initial selectivities again except for an increase concerning acetaldehyde and a decrease regarding the primary C_{2+Alc}, for which the differences also increased with higher chain-length, it can be concluded that the structural changes induced by the partial pressure variations mainly affected the Co–N–C sites catalysing the carbonylation of primary alcohols. Since specific characterisation of these sites is challenging due to the multitude of bulk Co-based species in the Mn_1Co_{11} catalyst, it can currently only be assumed that either the formation of these sites was negatively influenced, their anchoring on the carbon matrix deteriorated due to potential changes of its functionalization under the varied conditions or a combination of both effects led to the carbonylation pathway being less pronounced after the partial pressure variations. Furthermore, the diffraction pattern of the spent catalyst suggests sintering of the Co_2C phase during the steady-state kinetic investigations as well as formation of $MnCO_3$, which offers an additional explanation for the irreversible changes in catalytic performance induced by the performed parameter variations.

Comparing the PBA-based catalyst with the 2CoCu catalyst,[5] where Co_2C/Co^0 interface sites as well as metallic Co^0 resulted in product distributions described by the Anderson–Schulz–Flory (ASF) distribution, the deviating behaviour of PBA-derived catalysts, where the ASF distribution can no longer be applied to describe the oxygenate formation, must be attributed to the additional presence of the Co–N–C sites.[7,8] For further elucidation of the nature of the active sites in this study, the product gas stream was condensed in a cold trap during GHSV variations and revealed the presence of a volatile Co species. The information gained by this experiment strongly supports the proposed anchoring of Co atoms in the N-doped carbon matrix, resulting in the formation of Co–N–C sites catalysing the carbonylation of primary alcohols. However, a high partial pressure of water resulting from a high CO conversion was deemed detrimental for the molecular Co-based active site. Moreover, it was reported that very low concentrations of homogeneous Co species are active in hydroformylation, raising the question of whether the species trapped in the condensate

are also active for this reaction.[47] This question will be addressed in an upcoming study.

Future studies will also have the goal to selectively diminish the influence of the Co_2C/Co^0 interface sites and thus compare the influence of both active sites on the overall activity for oxygenate formation. These studies will involve the synthesis of single-atom catalysts (SACs) specifically containing Co–N–C sites with Co–N_4 moieties via a two-step pyrolysis of a hard template-based metal-coordinated polymer.[29] This will allow an unambiguous characterisation of these active sites and their catalytic activity under HAS conditions. Furthermore, the impact of Co–N–C sites can be further probed by co-feeding experiments with NH_3. The influence of this molecule at moderate pressures of 10 and 17 bar was recently investigated by Karroum et al.[48,49] for a Co–Mn-based catalyst.

As demonstrated by the high-pressure pulse experiments, the carbonylation pathway can be utilized to enhance the formation of higher alcohols by supplying additional MeOH. One possibility to continuously generate this alcohol as a starting point for the carbonylation cycle would be the addition of active sites for methanol synthesis to the PBA-derived catalyst, which, however, could interfere with its overall properties. An efficient way to circumvent such interferences while combining various catalytic functions was successfully demonstrated by the OXZEO concept, in which physical mixtures of an oxide and a zeolite were applied to selectively convert syngas to light olefins.[50] This concept has recently been applied in syngas conversion[51] and direct CO_2 hydrogenation[52] to higher alcohols, demonstrating that this approach has the potential to further improve the performance of PBA-derived catalysts based on the mechanistic insights originating from this work.

Conclusions

The transient and steady-state kinetics of the Mn_1Co_{11} catalyst were studied to obtain a deeper understanding of the interplay between the different HAS mechanisms comprising the carbide-based mechanism and reductive olefin hydroformylation over Co_2C/Co^0, reductive alcohol carbonylation over the molecular Co–N–C sites and olefin hydration over acidic sites.

The increase of the reaction temperature from 260 to 280 °C showed that low temperatures favour HAS, since the C_{2+Alc} selectivity was largest at 260 °C. Furthermore, irreversible changes concerning the product distribution occurred at 280 °C, shifting it to short-chain hydrocarbons presumably due to the sintering of metallic Co^0 nanoparticles. Furthermore, the variation of the GHSV clearly showed that the CO_2 selectivity can be directly linked to CO conversion due to the increasing amount of water being formed at high conversion. While the analysis of the reaction orders of CO and H_2 revealed a negative order for CO amounting to −0.2, a positive order of 0.7 was derived for H_2. A high partial pressure of H_2 promoted the formation of higher primary alcohols through the accelerated reduction of the intermediates formed via hydroformylation and especially carbonylation, and it also

led to an undesired shift towards short-chain hydrocarbons. Furthermore, the partial pressure variations showed clearly that the product distribution was irreversibly altered by an increased H_2/CO ratio, which is ascribed to detrimental changes of the molecular Co-based site resulting in decreased selectivities for all primary C_{2+Alc} compared with the initial state.

In situ DRIFTS investigations indicated the presence of Co mononitrosyl species at 160 °C, while the surface coverages changed during the heating phase leading to the exchange with CO. Investigation at 260 °C confirmed the presence of aldehydes and acids to a significant extent.

Ethylene co-feeding experiments showed that the reductive hydroformylation and the carbonylation of primary alcohols were not catalysed by the same Co-based active site, because the investigated mole fractions of ethylene resulted in distinct increases of the molar amounts of propionaldehyde and 1-PrOH, but not of long-chain primary alcohols.

High-pressure pulse experiments were applied to verify the proposed reaction network. The performed MeOH pulse series resulted in strong increases of the mole fractions of EtOH, 1-PrOH and 1-BuOH. This result not only demonstrates the reductive carbonylation of primary alcohols over Co–N–C sites, but it also suggests that this reaction is the dominant mechanism for the formation of higher alcohols under reaction conditions. Thus, Co–N–C sites are claimed to catalyse the reductive carbonylation of alcohols independently of the Co_2C/Co^0 interface sites. Leaching experiments further confirmed the presence of molecular Co–N–C sites due to an amount of 3.5 mg L^{-1} Co being present in the cold trap after 190 h TOS.

Author contributions

P. D.: formal analysis, investigation, validation, visualization, writing – review & editing; P. T.: conceptualization, formal analysis, investigation, visualization, writing – original draft; P. S.: conceptualization, formal analysis, investigation, visualization, writing – review & editing; A. M.: formal analysis, investigation, visualization, writing – review & editing; L. A.: investigation, writing – review & editing; M. M.: conceptualization, funding acquisition, resources, supervision, writing – review & editing.

Conflicts of interest

There are no conflicts to declare.

Data availability

Supplementary information is available: Comprising further spectral ranges of the shown DRIFTS measurements, more detailed information on the results of the steady-state kinetic experiments, additional high-pressure pulse experiments, details on the GC data evaluation, and basic characterization of the utilised catalyst. See DOI: **https://doi.org/10.1039/D5RE00268K**.

The data supporting this article have been included as part of the SI.

Notes and references

1 V. Thomas and A. Kwong, *Energy Policy*, 2001, **29**, 1133–1143.
2 Renewable Fuels Association, *Ethanol Industry Outlook 2016*, Washington, DC, 2016.
3 G. P. van der Laan and A. A. C. M. Beenackers, *Catal. Rev.: Sci. Eng.*, 1999, **41**, 255–318.
4 H. Schulz, T. Riedel and G. Schaub, *Top. Catal.*, 2005, **32**, 117–124.
5 C. Göbel, S. Schmidt, C. Froese, T. Bujara, V. Scherer and M. Muhler, *J. Catal.*, 2021, **394**, 465–475.
6 C. Göbel, S. Schmidt, C. Froese, Q. Fu, Y.-T. Chen, Q. Pan and M. Muhler, *J. Catal.*, 2020, **383**, 33–41.
7 P. Telaar, S. Schmidt, P. Diehl, P. Schwiderowski and M. Muhler, *ChemCatChem*, 2023, **15**, e202300357.
8 P. Telaar, P. Diehl, T. Herrendorf, S. Schaefer, W. Kleist and M. Muhler, *Catal. Sci. Technol.*, 2023, **13**, 6968–6980.
9 A. Jess and C. Kern, *Chem. Eng. Technol.*, 2009, **32**, 1164–1175.
10 V. Subramani and S. K. Gangwal, *Energy Fuels*, 2008, **22**, 814–839.
11 P. Telaar, P. Schwiderowski, S. Schmidt, S. Stürmer and M. Muhler, *ChemCatChem*, 2022, **14**, e202200385.
12 D. A. Bell, B. F. Towler and M. Fan, *Coal gasification and its applications*, Elsevier, Oxford, U.K, Burlington, MA, 2011.
13 M. K. Gnanamani, G. Jacobs, W. D. Shafer, D. E. Sparks, S. Hopps, G. A. Thomas and B. H. Davis, *Top. Catal.*, 2014, **57**, 612–618.
14 B. Zhang, C. Kubis and R. Franke, *Science*, 2022, **377**, 1223–1227.
15 C. Bai, A. Li, X. Yao, H. Liu and Y. Li, *Green Chem.*, 2016, **18**, 1061–1069.
16 T. Zhang, D. Zhang, X. Han, T. Dong, X. Guo, C. Song, R. Si, W. Liu, Y. Liu and Z. Zhao, *J. Am. Chem. Soc.*, 2018, **140**, 16936–16940.
17 R. V. Jagadeesh, H. Junge and M. Beller, *ChemSusChem*, 2015, **8**, 92–96.
18 J. Li, B. Wang, Y. Qin, Q. Tao and L. Chen, *Catal. Sci. Technol.*, 2019, **9**, 3726–3734.
19 J. Xian, S. Li, H. Su, P. Liao, S. Wang, Y. Zhang, W. Yang, J. Yang, Y. Sun, Y. Jia, Q. Liu, Q. Liu and G. Li, *Angew. Chem., Int. Ed.*, 2023, **62**, e202304007.
20 L. Osmieri, R. Escudero-Cid, A. H. Monteverde Videla, P. Ocón and S. Specchia, *Appl. Catal., B*, 2017, **201**, 253–265.
21 Q. Zhao, W. Yao, C. Huang, Q. Wu and Q. Xu, *ACS Appl. Mater. Interfaces*, 2017, **9**, 42734–42741.
22 M. Li, S. Wu, X. Yang, J. Hu, L. Peng, L. Bai, Q. Huo and J. Guan, *Appl. Catal., A*, 2017, **543**, 61–66.

23 X. Li, G. Lu, T. Wang, J.-Y. Yang, T. Herrendorf, P. Schwiderowski, J. Schulwitz, P. Chen, W. Kleist, G. Zhao, M. Muhler and B. Peng, *ChemSusChem*, 2024, **17**, e202300871.

24 X. Sun, A. I. Olivos-Suarez, D. Osadchii, M. J. V. Romero, F. Kapteijn and J. Gascon, *J. Catal.*, 2018, **357**, 20–28.

25 J. Li, D. Tu, J. Zhang, J. Li, Y. Xue, Q. Xu, Y. Du, C. Li and J. Lu, *Catal. Commun.*, 2020, **147**, 106138.

26 J. Masa, W. Xia, M. Muhler and W. Schuhmann, *Angew. Chem., Int. Ed.*, 2015, **54**, 10102–10120.

27 C. W. Bezerra, L. Zhang, K. Lee, H. Liu, A. L. Marques, E. P. Marques, H. Wang and J. Zhang, *Electrochim. Acta*, 2008, **53**, 4937–4951.

28 G. Wu and P. Zelenay, *Acc. Chem. Res.*, 2013, **46**, 1878–1889.

29 G. Lu, P. Schwiderowski, Z. Shen, X. Li, J. Schulwitz, B. Peng, G. Zhao, X. Huang and M. Muhler, *Chem. Mater.*, 2024, **36**, 2049–2060.

30 Y. Xiong, H. Li, C. Liu, L. Zheng, C. Liu, J.-O. Wang, S. Liu, Y. Han, L. Gu, J. Qian and D. Wang, *Adv. Mater.*, 2022, **34**, e2110653.

31 M. Zeng, Y. Liu, F. Zhao, K. Nie, N. Han, X. Wang, W. Huang, X. Song, J. Zhong and Y. Li, *Adv. Funct. Mater.*, 2016, **26**, 4397–4404.

32 J. Zhao, Y. He, F. Wang, W. Zheng, C. Huo, X. Liu, H. Jiao, Y. Yang, Y. Li and X. Wen, *ACS Catal.*, 2020, **10**, 914–920.

33 G.-L. Liu, T. Niu, A. Cao, Y.-X. Geng, Y. Zhang and Y. Liu, *Fuel*, 2016, **176**, 1–10.

34 P. Courty, D. Durand, E. Freund and A. Sugier, *J. Mol. Catal.*, 1982, **17**, 241–254.

35 M. F. Hertrich, F. K. Scharnagl, A. Pews-Davtyan, C. R. Kreyenschulte, H. Lund, S. Bartling, R. Jackstell and M. Beller, *Chem. – Eur. J.*, 2019, **25**, 5534–5538.

36 E. J. Moore, J. M. Sullivan and J. R. Norton, *J. Am. Chem. Soc.*, 1986, **108**, 2257–2263.

37 B. T. Baliga and E. Whalley, *Can. J. Chem.*, 1965, **43**, 2453–2456.

38 V. J. Nowlan and T. T. Tidwell, *Acc. Chem. Res.*, 1977, **10**, 252–258.

39 D. Laudenschleger, H. Ruland and M. Muhler, *Nat. Commun.*, 2020, **11**, 3898.

40 B. Mockenhaupt, P. Schwiderowski, J. Jelic, F. Studt, M. Muhler and M. Behrens, *J. Phys. Chem. C*, 2023, **127**, 3497–3505.

41 P. Schwiderowski, S. Stürmer and M. Muhler, *React. Chem. Eng.*, 2022, **7**, 2224–2230.

42 C. Drouet, P. Alphonse and A. Rousset, *Phys. Chem. Chem. Phys.*, 2001, **3**, 3826–3830.

43 B. H. Stuart, *Infrared spectroscopy. Fundamentals and applications*, Wiley, Chichester, 2004.

44 H. F. Shurvell, in *Handbook of vibrational spectroscopy*, ed. J. M. Chalmers and P. R. Griffiths, Wiley, Chichester, 2006.

45 A. H. Nielsen and H. H. Nielsen, *Phys. Rev.*, 1935, **48**, 864–867.

46 L. D. Almeida, A. R. Patiño, J. L. Cerrillo, S. Telalovic, L. Garzon-Tovar and J. Gascon, *ChemCatChem*, 2025, **17**, e202401482.

47 D. M. Hood, R. A. Johnson, A. E. Carpenter, J. M. Younker, D. J. Vinyard and G. G. Stanley, *Science*, 2020, **367**, 542–548.

48 H. Karroum, S. Chenakin, S. Alekseev, V. Iablokov, Y. Xiang, V. Dubois and N. Kruse, *ACS Catal.*, 2021, **11**, 14977–14985.

49 A. Raub, H. Karroum, M. Athariboroujeny and N. Kruse, *Catal. Lett.*, 2021, **151**, 613–626.

50 F. Jiao, J. Li, X. Pan, J. Xiao, H. Li, H. Ma, M. Wei, Y. Pan, Z. Zhou, M. Li, S. Miao, J. Li, Y. Zhu, D. Xiao, T. He, J. Yang, F. Qi, Q. Fu and X. Bao, *Science*, 2016, **351**, 1065–1068.

51 C. Huang, C. Zhu, M. Zhang, Y. Lu, Q. Wang, H. Qian, J. Chen and K. Fang, *ChemCatChem*, 2021, **13**, 3184–3197.

52 D. Xu, H. Yang, X. Hong, G. Liu and S. C. E. Tsang, *ACS Catal.*, 2021, **11**, 8978–8984.